AIMS Biophysics

http://www.aimspress.com/journal/biophysics/

AIMS Biophysics, 11(2): 142–165.
DOI: 10.3934/biophy.2024010
Received: 29 January 2024
Revised: 19 March 2024
Accepted: 25 March 2024
Published: 07 April 2024

Research article

Quantum chemical calculations on calcium oxalate and dolichin A and their binding efficacy to lactoferrin: An *in silico* study using DFT, molecular docking, and molecular dynamics simulations

Arjun Acharya[1], Madan Khanal[1], Rajesh Maharjan[1], Kalpana Gyawali[1], Bhoj Raj Luitel[2], Rameshwar Adhikari[3,4], Deependra Das Mulmi[5], Tika Ram Lamichhane[1,*] and Hari Prasad Lamichhane[1]

[1] Central Department of Physics, Tribhuvan University, Kathmandu 44600, Nepal

[2] Department of Urology and Kidney Transplant Surgery, Tribhuvan University Teaching Hospital, Institute of Medicine, Maharajgung, Kathmandu 44600, Nepal

[3] Central Department of Chemistry, Tribhuvan University, Kathmandu 44600, Nepal

[4] Research Center for Applied Science and Technology, Tribhuvan University, Kathmandu 44600, Nepal

[5] Nanomaterials Research Laboratory, Nepal Academy of Science and Technology, Lalitpur 44700, Nepal

* **Correspondence:** Email: tika.lamichhane@cdp.tu.edu.np.

Abstract: Lactoferrin, a member of the transferrin family, is one of the promoter proteins for calcium oxalate-type kidney stone formation. It exhibits a remarkable ability to interact with metals and oxalate ions. The prevalence of calcium oxalate in kidney stones was confirmed by the Fourier transform infrared spectra. The quantum chemical properties of calcium oxalate and dolichin A calculated by density functional theory and time-dependent density functional theory indicate their potential for hydrogen bonding and nonbonding interactions with the receptor proteins. From molecular docking analysis, the binding free energy of dolichin A was −7.78 kcal/mol, which was the best of twenty-four phytochemicals from *Macrotyloma uniflorum*, and that of calcium oxalate was −3.86 kcal/mol to lactoferrin. Furthermore, dolichin A having favorable physicochemical and pharmacokinetic properties offers post molecular dynamics molecular mechanics generalized Born surface area free energy of −17.61 ± 4.03 kcal/mol, indicating the strong binding interactions, and, therefore, it acts as a potential inhibitor of the lactoferrin.

Keywords: kidney stones; calcium oxalate and dolichin A; lactoferrin; density functional theory; protein-ligand interaction

1. Introduction

Urinary calculi, commonly known as kidney stones, are solid particles developed within the urinary system. Kidney stone disease frequently leads to severe pain, and it has the possibility of kidney failure in certain cases [1]. Currently, people have access to treatment procedures and preventive measures against urinary calculi; however, the prevalence of this disease is rapidly increasing in all developed and developing nations [2]. Urinary calculi have different chemical constituents, with the majority of them being calcium oxalate [3, 4]. Fourier transform infrared (FTIR) spectroscopy is a potential method for predicting the presence of calcium oxalate in these calculi [5]. The calcium oxalate molecule, consisting of one calcium and four electronegative oxygen atoms, has a possibility of hydrogen bond (H-bond) and nonbonded interactions with the proteins through the electric dipole and charge transfer process. Furthermore, these characteristics can be analyzed by computing various quantum chemical properties of compounds using the density functional theory (DFT) [6].

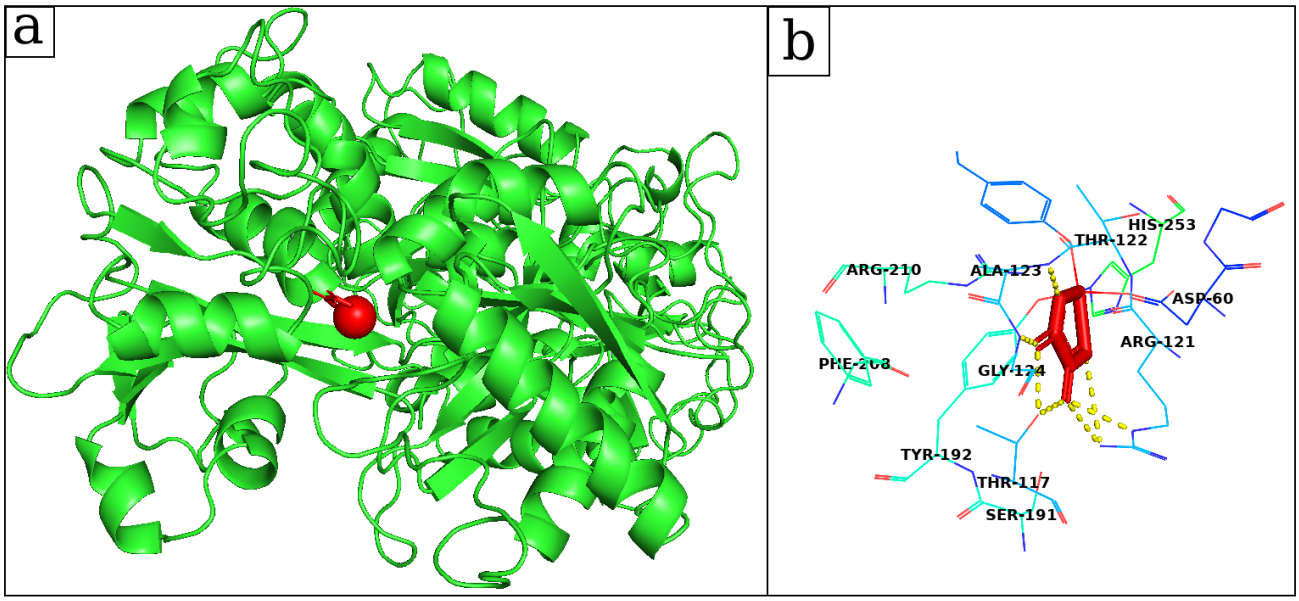

Figure 1. (a) Crystallographic structure of lactoferrin liganded with iron oxalate in red color (1BKA.PDB) and (b) representation of active residues of the lactoferrin with ligand iron oxalate in red color and hydrogen bonds in yellow broken lines using molecular visualizing software PyMOL.

In the process of forming calcium oxalate type kidney stones, which encompasses nucleation to aggregation, numerous proteins serve as promoters; however, the precise mechanism of urolithiasis is still unknown [7, 8]. Lactoferrin, a member of the transferrin family, is found in the kidney and matrix of urinary calculi [8, 9]. Experimental investigations of the kinetic rate of calcium oxalate monohydrate growth in the presence of lactoferrin have revealed its role as a growth promoter through progression of layers on the surfaces of crystals [8]. Lactoferrin also shows the internal flexibility to bind oxalate ions without significantly changing the polypeptide conformations. The first bounded anions create the proper binding site for the metal ions and there exits the synergistic relationship between anions and metal ions for the tight binding [10]. Arginine121 (ARG121),

Histidine253 (HIS253), Aspartic acid60 (ASP60), Tyrosine192 (TYR192), Serine191 (SER191), Arginine210 (ARG210), Phenylalanine208 (PHE208), Threonine117 (THR117), Glycine124 (GLY124), Alanine123 (ALA123), and Threonine122 (THR122) exhibit the active residues in the binding site of the lactoferrin (Figure 1). Therefore, calcium oxalate is one of the metal oxalates that can also bind with the active residues of lactoferrin and promotes the formation of calcium oxalate type kidney stones. The different phytocompounds play the inhibitory roles against the urinary proteins promoting urolithiasis [11–13]. *Macrotyloma uniflorum* (*M. uniflorum*) has been traditionally used for the treatment of kidney stone disease. Experimental studies identified that the legumes of *M. uniflorum* show the antilithiatic properties [14–16]. The potential bioactive compounds of *M. uniflorum* can inhibit the lactoferrin by the strong interactions with the residues in its oxalate binding site. The interactions between protein and ligand can be investigated by means of molecular docking and molecular dynamics (MD) simulations following molecular mechanics energies combined with the generalized Born and surface area continuum solvation (MM-GBSA) approach [17–19].

This research aims to investigate the quantum chemical properties of calcium oxalate and dolichin A (an effective phytochemical from *M. uniflorum*), along with their possible interactions within the active region of lactoferrin. The druglikeness of dolichin A and its conformational stability in complex with lactoferrin have been analyzed. The present study explores the understanding of the promoting role of lactoferrin and contributes to the development of a drug candidate against calcium oxalate induced kidney stone disease.

2. Materials and methods

2.1. FTIR characterization

Kidney stones were obtained from the Tribhuvan University Teaching Hospital following the receipt of approval from the Institutional Review Committee of the Institute of Medicine, Tribhuvan University, Kathmandu, Nepal. Surgically removed eleven samples were collected from 1 September 2022 to 1 March 2023, ensuring an unbiased selection process. Informed consent was obtained from all participants, including parents or legal guardians of minors, to allow for the collection and analysis of the kidney stones. The collected samples were meticulously cleaned with distilled water and subsequently air-dried at room temperature. Subsequently, the kidney stones were crushed using a stainless steel mortar and pestle. FTIR spectroscopy was employed for sample characterization in the spectral range of 400-4000 cm^{-1} using a SHIMADZU IRAffinity-1S spectrophotometer.

2.2. Gaussian calculations

The initial structures of calcium oxalate (Compound ID 33005) and dolichin A (Compound ID 44257432) were obtained from the PubChem database. These molecules were optimized using the DFT method at the Becke 3-parameter; Lee, Yang, Parr (B3LYP)/6-311++G(d,p) level of calculation in Gaussian 16W software [20]. From the optimized molecular structures, various molecular properties including the dipole moment, Mulliken charges, molecular electrostatic potential (MEP), highest occupied molecular orbital (HOMO) and lowest unoccupied molecular orbital (LUMO),

global reactivity descriptors, and density of states (DOS) were computed in the gas phase. Additionally, infrared intensities in both the gas phase and water solvent using the integral equation formulation of the polarizable continuum model (IEFPCM) and thermodynamic properties in the gas phase of the calcium oxalate molecule were calculated using the DFT method at the same level of calculation. Furthermore, ultraviolet-visible (UV-Vis) spectra were also generated using the time-dependent (TD)-DFT method at the same level of calculation [20]. For visualization and in-depth analysis, GaussView 6 [21], GaussSum 3.0 [22], and VEDA4 software were utilized [23].

2.3. Molecular docking

Crystallographic structure of lactoferrin (1BKA.PDB) was downloaded from https://www.rcsb.org [10] and refined using SWISS-MODEL [24], resulting in a template with global model quality estimate (GMQE) and distance constraints applied on model quality estimation (QMEANDisCo) global scores of 0.93 and 0.88 ± 0.05, respectively. Employing literature sources [25–28], twenty-four distinct chemicals present in *M. uniflorum* were primarily selected as ligands. These chemical compounds were downloaded in sdf format from the PubChem database [29]. Notably, among the selected compounds, dolichin A exhibited the best binding score within the active domain of lactoferrin as determined using PyRx software [30]. In the preparation of molecular docking using AutoDock4, removal of water molecules, addition of Kollmann's charges, integration of polar hydrogen atoms, and conversion of protein data bank (PDB) to protein data bank with partial charge and atom type (PDBQT) format for the proteins and ligand were performed using the graphical user interface of AutoDockTools [31, 32]. In this conversion process, partial atomic charges and atom types were added to the receptor proteins [33]. The atomic affinity potential of each atom of ligands with proteins was calculated using the AutoGrid process. Molecular docking was performed using grid points (34 × 30 × 30) and (50 × 50 × 50) for calcium oxalate and dolichin A along the x, y, and z axes, respectively. Out of several search methods in molecular docking, the Lamarckian genetic algorithm was applied for the protein and ligand [34]. A large number of conformations were developed and the best solution was obtained after analyzing the different predicted energies of the conformations [34]. To ensure exhaustiveness in the conformational search, a maximum of 2,500,000 energy evaluations were performed, and a number of individuals in the population was set to 300. Additionally, the maximum number of generations was set to 27,000, and the number of docking procedures was extended to 100 [32, 34–36]. For validation purposes, the DockRMSD online tool was utilized to calculate the root mean square deviation (RMSD) between the generated coordinates of the docked ligand and the original coordinates of the native one [37]. The protein-ligand interactions were analyzed using PyMOL 2.5.2 [38], LigPlot+ v.2.2 [39], and BIOVIA Discovery Studio Visualizer v21.1.0.20298 [40].

2.4. Molecular dynamics simulations

The protein-ligand complex having the best binding scores from molecular docking was subjected to MD simulations using GROMACS 2019.6 [41]. The ligand dolichin A was parameterized using the SwissParam online tool [42]. The simulations employed the chemistry at Harvard macromolecular mechanics (CHARMM) force field, using the CHARMM27 parameter set [43] and the complexes were solvated using the transferable intermolecular potential with a 3 points (TIP3P) water

model [44]. Neutralization was achieved by adding Na^+ and Cl^- ions followed by a 50,000-step minimization using the steepest descent method. Prior to the production run, the system was equilibrated in the constant-temperature, constant-volume (NVT) ensemble with temperature control using the V-rescale (modified Berendsen thermostat). Again, a subsequent equilibration was performed in the constant-temperature, constant-pressure (NPT) ensemble, employing the V-rescale thermostat and isotropic Berendsen pressure coupling. Finally, production runs for MD simulation were performed using the V-rescale thermostat and Parrinello-Rahman barostat, maintaining a constant temperature of 300 K and pressure of 1 bar for a duration of 100 ns with a time step of 1 fs. Trajectories were recorded every 0.1 ns, and conformational changes were analyzed through RMSD, root-mean-square-fluctuation (RMSF), radius of gyration (R_g), solvent accessible surface area (SASA), and H-bond interactions [19].

2.5. Druglikeness and toxicity prediction

The evaluation of physicochemical, lipophilic, pharmacokinetic, and druglikeness parameters and toxicity of dolichin A, based on its canonical simplified molecular input line entry system in PubChem, was performed using the SwissADME tool, admetSAR 2.0, and ProTox-II [45–47].

2.6. MM-GBSA calculations

The open source packages for Groningen machine for chemical simulations (GROMACS), gmx_MMPBSA and gmx_MMPBSA_ana were used to analyze the binding free energy contributors in lactoferrin-dolichin A conformers during MD simulations [48]. The binding free energy of the protein-ligand complex (ΔG_{bind}) is calculated using Equation 2.1 [18]

$$\Delta G_{bind} = G_{PL} - (G_P + G_L) \tag{2.1}$$

where, G_{PL} is the bound free energy of the protein-ligand complex, whereas G_P and G_L are the unbound free energies of protein and ligand, respectively.

3. Results and discussion

3.1. Geometry optimization

Calcium oxalate and dolichin A were optimized by the DFT method at the B3LYP/6-311++G(d,p) level of calculation. The optimized structures have been shown in Supplementary Figure 1S. The calculated dipole moments of calcium oxalate and dolichin A are found 14.880 Debye and 4.264 Debye, respectively. Dipole-dipole interactions between protein and ligand can affect the binding energy of the system [49]. So, these compounds can also interact through dipole-dipole interactions with proteins related to nephrolithiasis.

3.2. Frontier molecular orbitals

Electronic absorption spectra were obtained using the TD-DFT method at the B3LYP/6-311++G(d,p) level of calculation (Figure 2a,b). The wavelengths of 335 nm, 406 nm, and 507 nm are responsible for the electronic transition of calcium oxalate. Among these transitions,

the maximum oscillatory strength is observed for wavelength 507 nm due to major contribution from the electron donor (HOMO) to electron acceptor (LUMO) transition of electrons (Table 1). Again, wavelengths of 268 nm, 265 nm, and 278 nm are observed for dolichin A. The wavelength of 271 nm is due to the transition of HOMO to LUMO+1, and HOMO to LUMO+2 shows maximum oscillatory strength (Table 1).

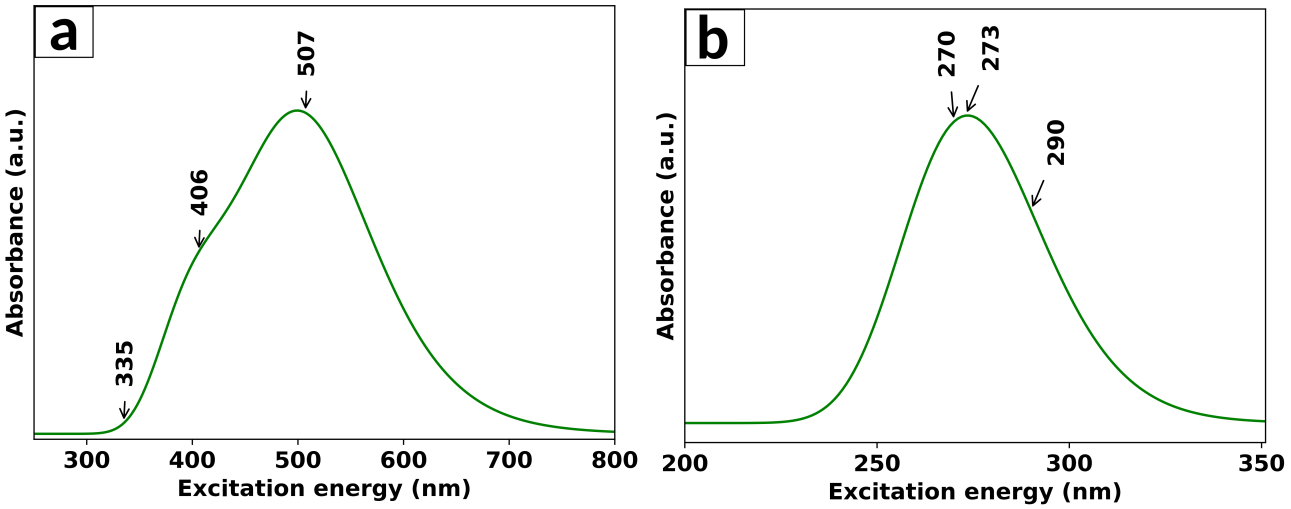

Figure 2. Calculated electronic absorption spectra of (a) calcium oxalate and (b) dolichin A.

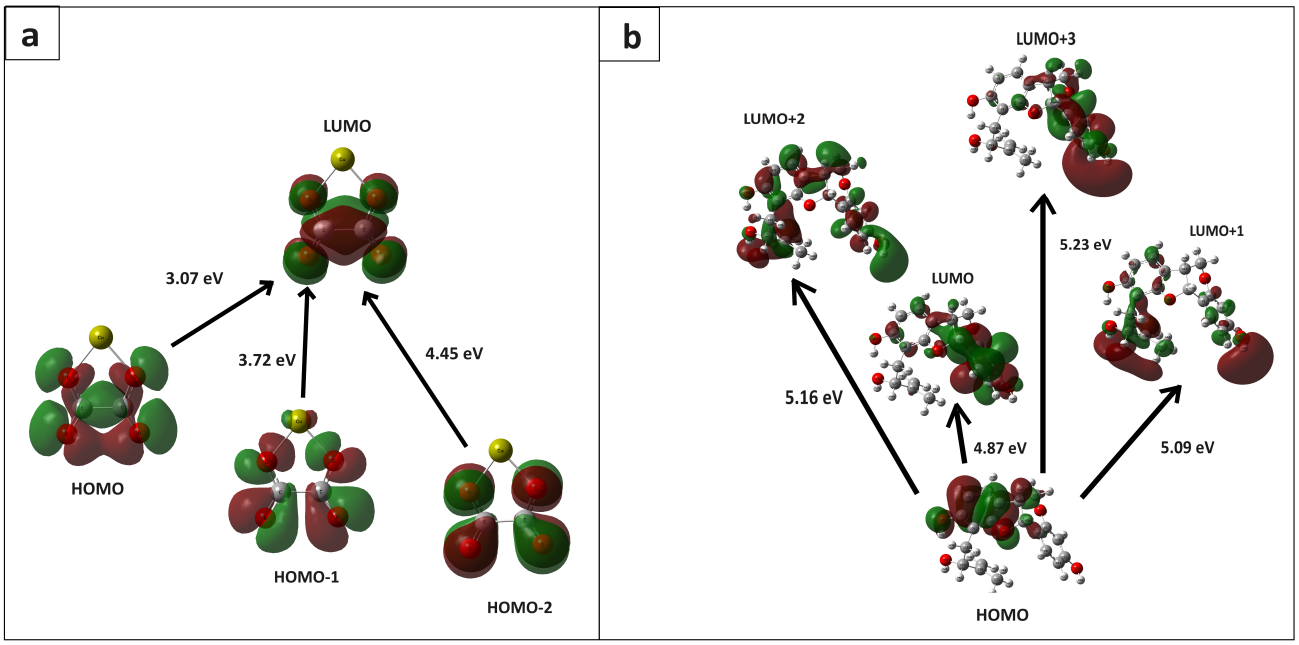

Figure 3. The frontier molecular orbitals significantly contributing to the electronic transitions in (a) calcium oxalate and (b) dolichin A.

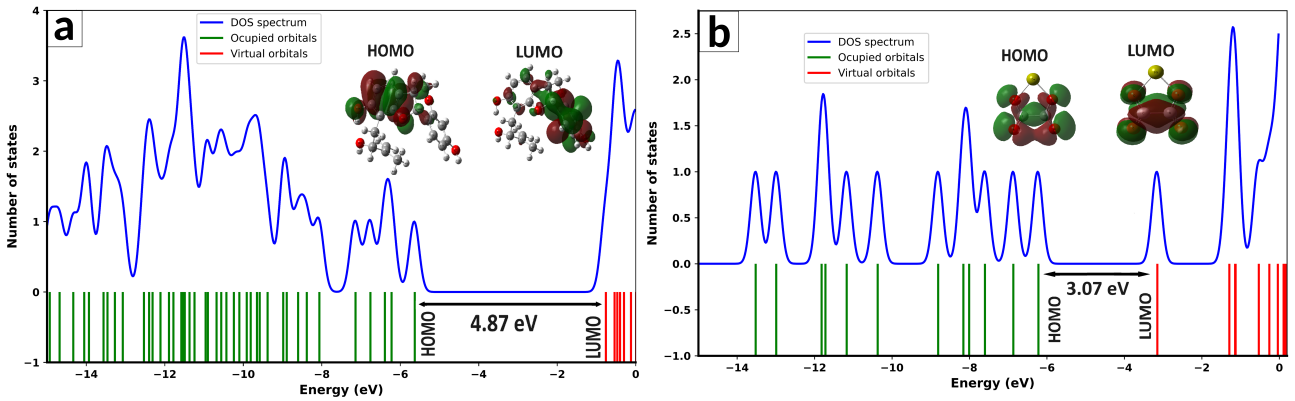

Figure 4. DOS in both occupied and virtual orbitals in (a) calcium oxalate and (b) dolichin A.

In the frontier molecular orbitals (Figure 3), the green and red regions surrounding the atoms correspond to negative and positive charge phases, respectively [50]. In the case of calcium oxalate, a significant portion of the charge density is predominantly localized around the carbon and oxygen atoms, as shown in Figure 3a. In dolichin A, there is a noticeable shift in charge density from one molecular orbital region to another, as visualized in Figure 3b. This visual representation effectively conveys the nature of charge distribution within the molecule [51]. The energy gaps, represented as the difference between E_{HOMO} and E_{LUMO}, are found to be 3.07 eV and 4.87 eV for calcium oxalate and dolichin A, respectively (Figure 3). The number of states per unit energy interval at a given energy level in both occupied and virtual orbitals for calcium oxalate and dolichin A are illustrated with the DOS spectrum in Figure 4. The HOMO-LUMO orbitals (Figure 3) and the spectra of DOS (Figure 4) show good agreement with each other. These results indicate that both calcium oxalate and dolichin A can facilitate charge transfer process and have enhanced potential for biological activities [52].

Table 1. Calculated electronic properties of calcium oxalate and dolichin A.

Compounds	Maxiumum absoption wavelength (nm)	Oscillatory strength	Major contributions
Calcium oxalate	507	0.014	HOMO → LUMO (99%)
	406	0.007	HOMO-1 → LUMO (99%)
	335	0.000	HOMO-2 → LUMO (99%)
Dolichin A	289	0.008	HOMO→LUMO (97%)
	271	0.049	HOMO→LUMO+1 (64%), HOMO→LUMO+2 (10%)
	268	0.009	HOMO→LUMO+2 (64%), HOMO→LUMO+3 (27%)

3.3. Global reactivity descriptors

The ionization potential ($I = -E_{HOMO}$) and electron affinity ($A = -E_{LUMO}$) of calcium oxalate were calculated using Koopmans' theorem [53]. The global reactive descriptors of the chemical can be predicted by the chemical hardness ($\eta = (I - A)/2$), chemical softness ($S = 1/\eta$), electronic chemical

potential ($\mu = -(I + A)/2$), and global electrophilicity index ($\omega = \mu^2/(2\eta)$) [53–55]. Calcium oxalate and dolichin A show positive values for chemical hardness and electrophilicity index (Table 2). This observation suggests that the compounds are suitable for charge transfer processes and can impact the binding energy in protein-ligand interactions [56]. Furthermore, the chemical softness of calcium oxalate (0.65 per eV) is found to be higher in comparison with dolichin A (0.41 per eV), which suggests calcium oxalate is more reactive than dolichin A [52].

Table 2. Calculated global reactivity descriptors of calcium oxalate and dolichin A.

Compounds	Ionization potential (I) (eV)	Electron affinity (A) (eV)	Chemical hardness (η) (eV)	Chemical softness (S) (eV)$^{-1}$	Electronic chemical potential (μ) (eV)	Global electrophilicity index (ω) (eV)
Calcium oxalate	6.22	3.15	1.54	0.65	−4.68	7.15
Dolichin A	5.56	0.68	2.44	0.41	−3.12	1.99

3.4. Molecular electrostatic potential and Mulliken atomic charges

MEP map and Mulliken atomic charge are helpful for the interpretation of reactive behavior of the molecules related to electrophilic and nucleophilic attacks [57]. The visual representation of MEP shows the relative polarities within the calcium oxalate and dolichin A molecules (Figure 5). In the MEP map, an increase in electrostatic potential regions corresponds to the order red < yellow < green < blue, with the color codes ranging from −0.273 a.u. to 0.273 a.u. for calcium oxalate and from −0.121 a.u. to 0.121 a.u. for dolichin A, respectively. Within the calcium oxalate molecule, relative positive potential region is observed in the vicinity of calcium atom, while relative negative potential regions are concentrated around oxygen atoms. In dolichin A, relative positive potential regions are found around hydrogen atoms, while relative negative potential regions are found around oxygen atoms. Both positive and negative potential regions are also present around the carbon atoms. The distribution of Mulliken atomic charges of calcium oxalate and dolichin A molecules are shown in Figure 6. In calcium oxalate, the Ca7 atom shows the maximum positive Mulliken atomic charge. Ca7 is bonded to O1 and O4 oxygen atoms, resulting in the induction of more negative charges on the oxygen atoms O1 and O4 than that of O2 and O3 (Table 1S). In dolichin A, all hydrogen atoms exhibit positive Mulliken atomic charges, while all oxygen atoms show negative Mulliken atomic charges (Table 1S). Carbon atoms in calcium oxalate show positive Mulliken atomic charges, whereas in dolichin A, carbon atoms exhibit both positive and negative Mulliken atomic charges. From the MEP and Mulliken atomic charge distributions, calcium oxalate and dolichin A molecules show the polar properties, and these electrophilic and nucleophilic sites interact with the lactoferrin (Figure 2S).

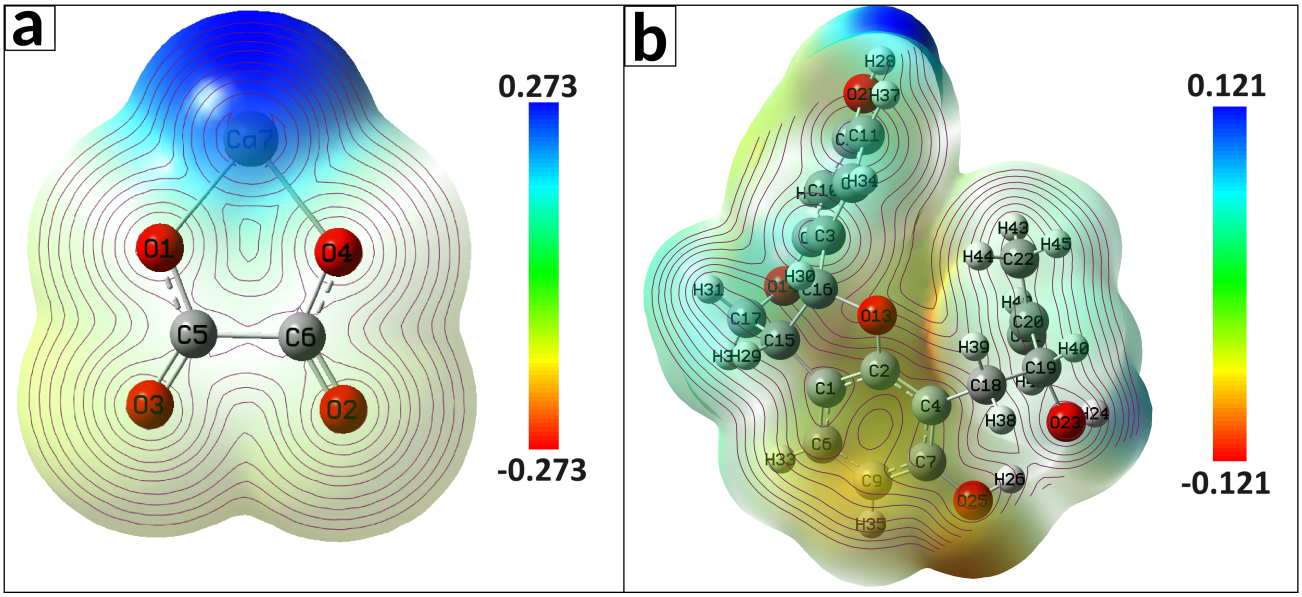

Figure 5. MEP map with contour lines (a) calcium oxalate and (b) dolichin A.

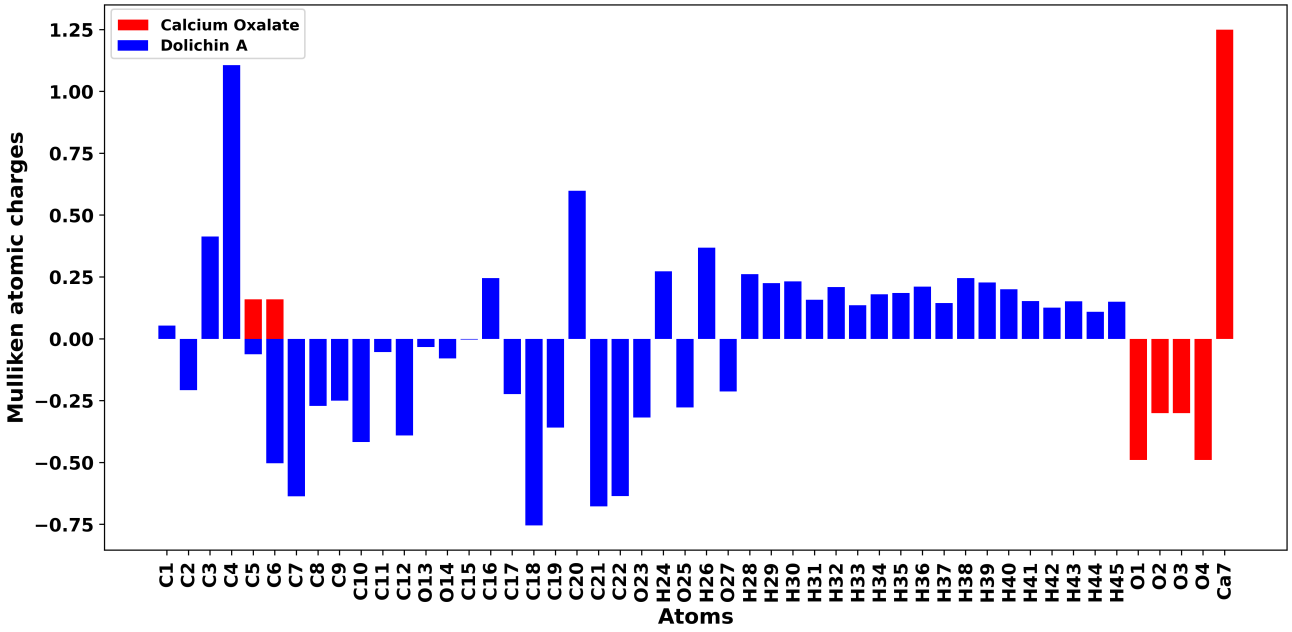

Figure 6. Mulliken atomic charge distributions of calcium oxalate and dolichin A.

3.5. Vibrational analysis

Calcium oxalate has seven atoms with fifteen modes (3N-6) of vibration [58]. The calculated vibrational frequencies (scaled and unscaled) compared with the experimental results in the gas phase and the water solvent along with potential energy distribution (PED) are shown in Tables 3 and 4. Due to the presence of a calcium atom, the bond strength between (O1-C5) and (O4-C6) becomes weaker than (O2-C6) and (O3-C5). So, the frequencies of (O1-C5) and (O4-C6) have been downshifted by 533 cm^{-1} in symmetric and by 651 cm^{-1} in asymmetric stretching, with respect to corresponding

modes of (O2-C6) and (O3-C5) in the gas phase (Table 3). Furthermore, frequencies of (O1-C5) and (O4-C6) have been downshifted by 255 cm^{-1} in symmetric stretching and by 347 cm^{-1} in asymmetric stretching, with respect to corresponding modes of (O2-C6) and (O3-C5) in the water solvent (Table 4). The calculated frequencies are uniformly scaled by using the wavenumber linear scaling procedure as: $\nu_{\text{observed}} = \nu_{\text{calculated}} \times (1.0087 - 0.0000163\ \nu_{\text{calculated}})$ for the DFT method at the B3LYP/6-311++G(d,p) level of calculation [59].

Table 3. Calculated vibrational analysis of calcium oxalate along with potential energy distribution in the gas phase, available experimental FTIR results of calcium oxalate monohydrate, and FTIR results of kidney stones.

Calc. FTIR intensity	Calc. Freq. (unscaled) cm^{-1}	Calc. Freq. (scaled) cm^{-1}	Exp. FTIR freq. cm^{-1} [5]	Exp. FTIR freq. cm^{-1}	Assignment [PED (>10%)]
1901.32	1800	1763			ν[O2-C6 & O3-C5](93)
261.07	1782	1746	1618	1609	ν_a[O2-C6 & O3-C5](91)
1498.56	1245	1230	1317	1383	ν[O1-C5 & O4-C6](75)
374.46	1105	1095		1314	ν_a[O1-C5 & O4-C6](76), δ_a[(O2-C6-O4) & (O1-C5-O3, C5-O1-Ca7 & C6-C5-O1)](14)
348.09	856	852			ν[O1-C5 & O4-C6](11), ν_a[C5-C6 & Ca7-O1](17), δ[O2-C6-O4 & O1-C5-O3](62)
0.00	833	829			γ[O2-C5-O4-C6 & O3-C6-O1-C5](97)
522.08	784	781			ν_a[O1-C5 & O4-C6](11), δ_a[(O2-C6-O4) & (O1-C5-O3, C5-O1-Ca7 & C6-C5-O1)](72)
435.81	554	553			ν[Ca7-O1](80)
30.10	543	543			δ_a[C6-C5-O1 & C5-C6-O4](79), ν_a[O1-C5 & O4-C6](11)
433.46	493	493			γ_a[O2-C5-O4-C6 & O3-C6-O1-C5](90)
416.55	370	371			ν_a[C5-C6 & Ca7-O1](24), δ [C5-O1-Ca7, C6-C5-O1, C5-C6-O4 & O2-C6-O4](50)
472.06	364	365			ν_a[C5-C6 & Ca7-O1](36), δ[O2-C6-O4 & O1-C5-O3](17), δ [C5-O1-Ca7, C6-C5-O1, C5-C6-O4 & O2-C6-O4](30)
46.43	321	322			δ_a[C5-O1-Ca7 & C5-C6-O4](85)
779.45	118	119			τ[Ca7-O1-C5-C6](90)
0.00	52	52			τ[O4-C6-C5-O1](97)

Symbols: ν, δ, τ and γ represent the stretching, bending, torsion and out-of-plane modes of symmetric vibrations, respectively, and the subscript "a" represents the corresponding asymmetric mode for each mode of vibration. Abbreviations: Calc.,Exp. and Freq. represent calculated, experimental and frequency, respectively.

Table 4. Calculated vibrational analysis of calcium oxalate along with potential energy distribution in the water solvent, available experimental FTIR results of calcium oxalate monohydrate, and FTIR results of kidney stones.

Calc. FTIR intensity	Calc. Freq. (unscaled) cm^{-1}	Calc. Freq. (scaled) cm^{-1}	Exp. FTIR freq. cm^{-1} [5]	Exp. FTIR freq. cm^{-1}	Assignment [PED (>10%)]
4719.19	1645	1615			ν[O2-C6 & O3-C5](83), ν[O1-C5 & O4-C6](12)
253.03	1637	1608	1618	1609	ν_a[(O4-C6 & O1-C5) & O3-C5](86)
1540.01	1379	1360	1317	1383	ν[O1-C5 & O4-C6](72), ν[C5-C6](13)
1044.70	1277	1261		1314	ν_a[O4-C6 &(O1-C5, O3-C5)] (89)
172.24	871	866			δ[O2-C6-O4 & O1-C5-O3] (49) ν[O1-C5 & O4-C6](12), ν[C5-C6](17)
0.22	859	855			γ[O2-C5-O4-C6 & O3-C6-O1-C5](98)
904.65	772	769			δ[O1-C5-O3](82)
128.24	573	573			ν_a[(O4-C6 & O1-C5) & O3-C5](11), γ_a[O2-C5-O4-C6](21), δ[C6-C5-O1](60)
556.00	481	481			γ[O2-C5-O4-C6](80), δ[C6-C5-O1](12)
372.20	476	477			δ[O1-C5-O3 & O2-C6-O4] (30), ν[C5-C6](59)
417.29	344	345			δ[C5-C6-O4, C6-C5-O1, O2-C5-O4 & O1-C5-O3](82)
2679.31	275	276			ν_a[C5-C6 & Ca7-O1](44), δ[C5-O1-Ca7](36)
911.14	256	257			ν_a[C5-C6 & Ca7-O1](41), δ[C5-O1-Ca7](44)
1318.69	102	103			τ[C6-C5-O1-Ca7](95)
6.68	82	83			τ[O1-C5-C6-O4](97)

In the gas phase, symmetric stretching of (O2-C6) and (O3-C5) and that of (O1-C5) and (O4-C6) with a minor contribution from the bending modes of (O2-C6-O4 and O1-C5-O3) (Table 3), are

responsible for the most intense FTIR intensity at frequencies 1763 cm^{-1}, and 1230 cm^{-1}, respectively (Figure 3S). In the water solvent, the most intense FTIR spectra are observed at frequencies of 1615 cm^{-1}, 1360 cm^{-1} and 1261 cm^{-1} (Figure 7c). The frequency of 1615 cm^{-1} is due to the symmetric stretching of all (O-C) bonds. The frequency of 1360 cm^{-1} is due to the symmetric stretching of (O1-C5) and (O4-C6) with a minor contribution by stretching of (C5-C6). The frequency of 1261 cm^{-1} is contributed by the asymmetric stretching of (O1-C5) with (O2-C6) and (O4-C6) (Table 4).

3.6. Experimental FTIR analysis of kidney stones

Out of eleven samples, FTIR spectra of eight samples having similar patterns have been considered for further analysis (Figure 7). Average values with standard deviations of major peaks are observed at 1609 ± 1 cm^{-1}, 1383 ± 1 cm^{-1}, and 1314 ± 1 cm^{-1}. FTIR spectra of calcium oxalate in the gas phase and in the tetrahydrofuran (THF), carbon tetrachloride (CCl_4), and water solvents were calculated at the B3LYP/6-311++G(d,p) level of calculation (Figure 4S). The calculated FTIR spectrum in the water solvent nearly matches with the experimental FTIR peaks (Figure 7) and also with the peaks reported for calcium oxalate monohydrate [5].

3.7. Thermodynamic properties

The thermodynamic properties of compounds are intricately linked with their interactions with the target proteins [60]. The variation of thermal energy correction (E), molar heat capacity at constant volume (C_V), and entropy (S) of calcium oxalate in the gas phase with temperatures ranging from 50 K to 500 K with an increment of 50 K are presented in Table 2S. The correlation equations of thermal energy correction, molar heat capacity at constant volume, and entropy are found as:
Thermal energy (E) = 16.04170 + 0.00567 T + 0.00003 T^2
Heat capacity (C_V) = 5.66920 + 0.05303 T - 0.00001 T^2
Entropy (S) = 48.52010 + 0.16623 T - 0.00018 T^2
Based on the correlation graph best fitted with the coefficient of determining of nearly one, each of the three calculated thermodynamic parameters shows an increasing trend with temperature (Figure 8). This behavior is due to the rise in the vibrational intensities of molecules with increasing temperature [61].

3.8. Molecular docking

The protein-ligand complexes of lectoferrin with calcium oxalate and dolichin A were generated using molecular docking. For the validity of the molecular docking, the native ligand FeC_2O_4 was extracted from the lactoferrin receptor (1BKA.PDB) and redocked in the vicinity of its original position using AutoDock4.2 (Figure 5S). The RMSD of the generated coordinates of docked ligand from its original coordinates is found at 0.208 Å, and such validated setup was used in molecular docking of calcium oxalate and dolichin A into the lactoferrin.

The molecular docking of calcium oxalate in the vicinity of the metal-oxalate binding regions of the lactoferrin results the binding energy of −3.86 kcal/mol (Table 5). Specifically, residues ARG121 and ASP60 form H-bonds, and the residues PHE63, PHE183, Leucine59 (LEU59), and Proline42 (PRO42) engage in hydrophobic interactions with calcium oxalate (Table 6).

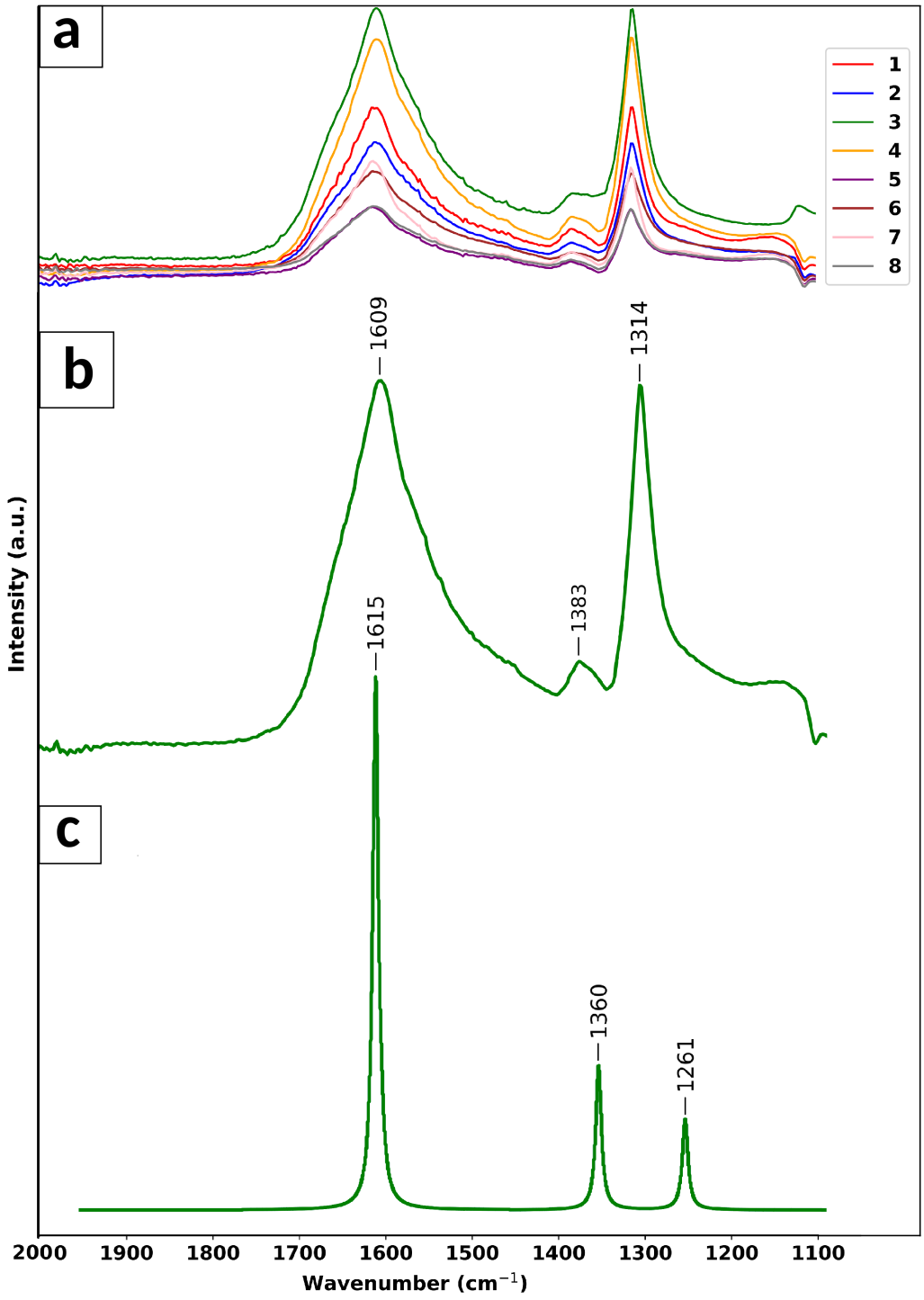

Figure 7. (a) Experimental FTIR spectra of kidney stone samples, (b) FTIR spectrum of the average intensity of 8 kidney stone samples, and (c) calculated FTIR spectrum of calcium oxalate in the water solvent.

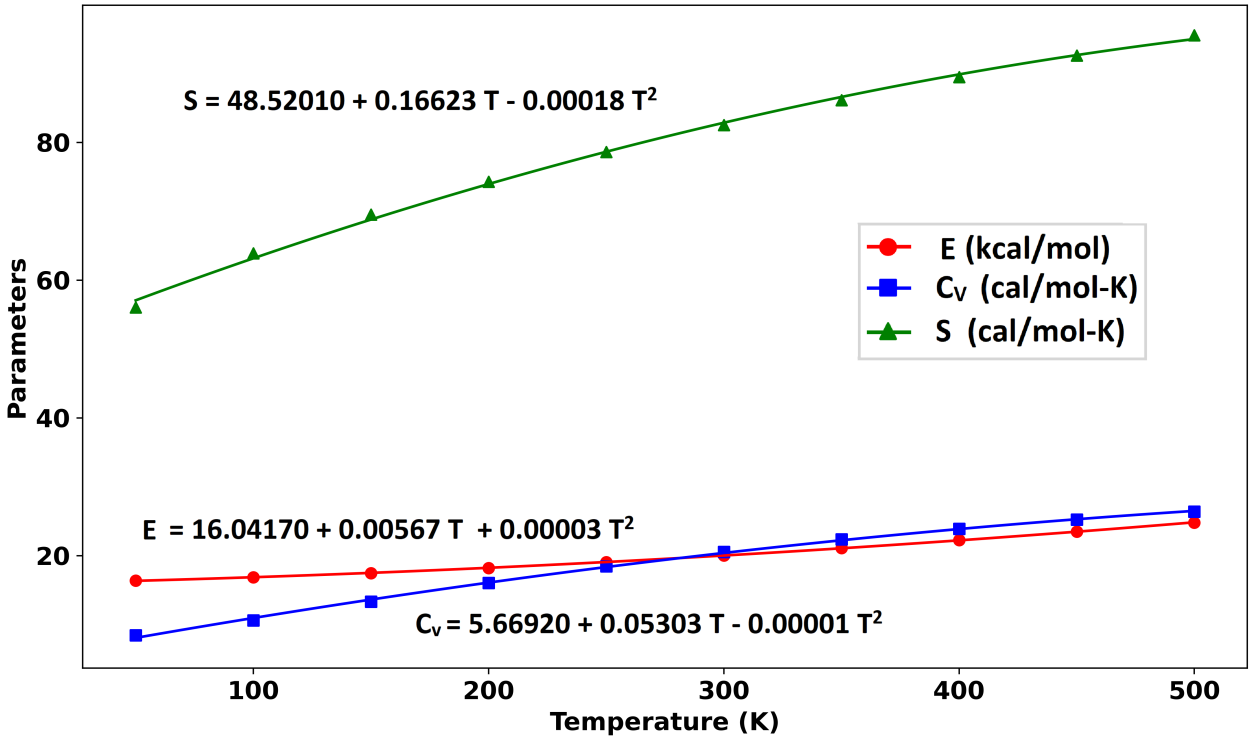

Figure 8. Variation of thermal energy correction (E), molar heat capacity at constant volume (C_V), and entropy (S) with temperature of calcium oxalate in the gas phase.

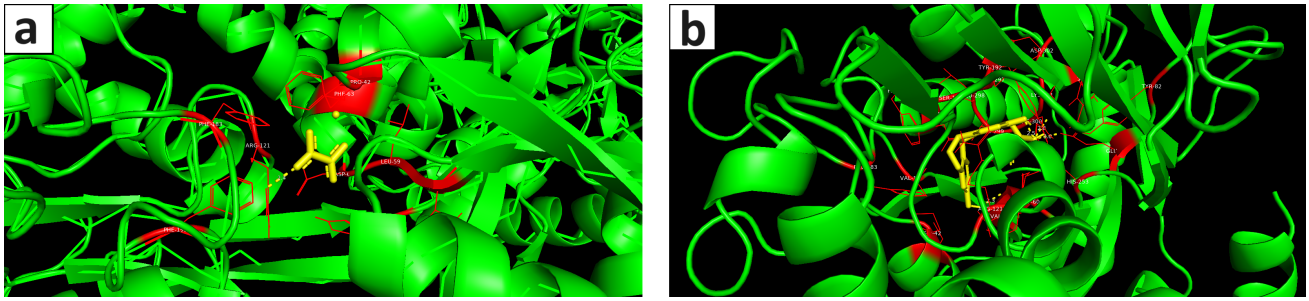

Figure 9. Three-dimensional representation of the binding domain of lactoferrin interacting with (a) calcium oxalate and (b) dolichin A using PyMOL. The ligands and interacting residues are shown in yellow and red colors, respectively.

Table 5. Molecular docking results of calcium oxalate and dolichin A with lactoferrin at temperature 298.15 K.

Compounds	Final intermolecular energy [vdW + H-bond + desolv+electrostatic energy] (kcal/mol)	Final total internal energy (kcal/mol)	Torsional free Energy (kcal/mol)	Unbound system's energy (kcal/mol)	Estimated free energy of binding (kcal/mol)
Calcium oxalate	−3.86	0.00	0.00	0.00	−3.86
Dolichin A	−9.57	−1.69	+1.79	−1.69	−7.78

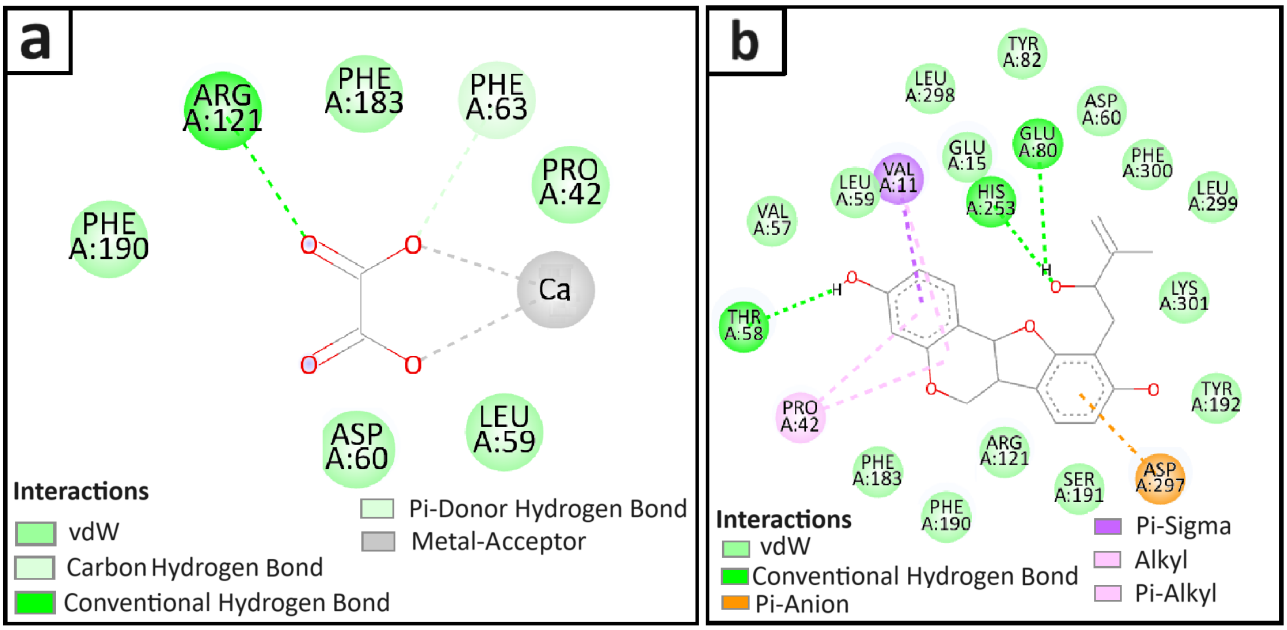

Figure 10. Two-dimensional visualization of the interactions of lactoferrin with (a) calcium oxalate and (b) dolichin A using BIOVIA Discovery Studio.

Table 6. Active residues of lactoferrin and their interactions with calcium oxalate and dolichin A in the best docked pose after molecular docking.

	Active amino acids	Types of interaction	Interacting atoms (Receptor – ligand)	Bond length (Å)
Calcium oxalate	ARG121	H-bond	NH1 – O4	3.02
	ASP60	H-bond	N – O2	3.04
	PHE63, PHE183, LEU59, PRO42	Non-bonded		
Dolichin A	HIS253	H-bond	ND1 – O3	3.08
	HIS253	H-bond	ND1 – O4	2.95
	GLU80	H-bond	OE2 – O4	3.03
	THR58, ASP297, ARG121, PHE300, LYS301,GLU15, VAL11, VAL57, LEU59, PRO42, PHE190, SER191, TYR192, LEU299	Non-bonded		

The binding energies of twenty-four chemicals found in *M. uniflorum* [25–28] and two-dimensional docking images at the oxalate binding site of lactoferrin are presented in Table 3S and Figures 6S and 7S. Among all compounds, dolichin A exhibits the strongest binding affinity with the lactoferrin resulting in the binding energy of −7.78 kcal/mol (Table 5). The residues HIS253 and Glutamic acid80 (GLU80) form the H-bonds whereas the residues THR58, ASP297, ARG121, PHE300, LYS301, GLU15, ASP60, Valine11 (VAL11), VAL57, LEU59, PRO42, PHE190, SER191,

TYR192, and LEU299 perform hydrophobic interactions with dolichin A (Table 6). Three-dimensional and two-dimensional visualizations of calcium oxalate and dolichin A in complex with lactoferrin are shown in Figures 9, 10, and 2S. The results of molecular docking show that dolichin A is a potential inhibitor of the lactoferrin.

3.9. Molecular dynamics simulations

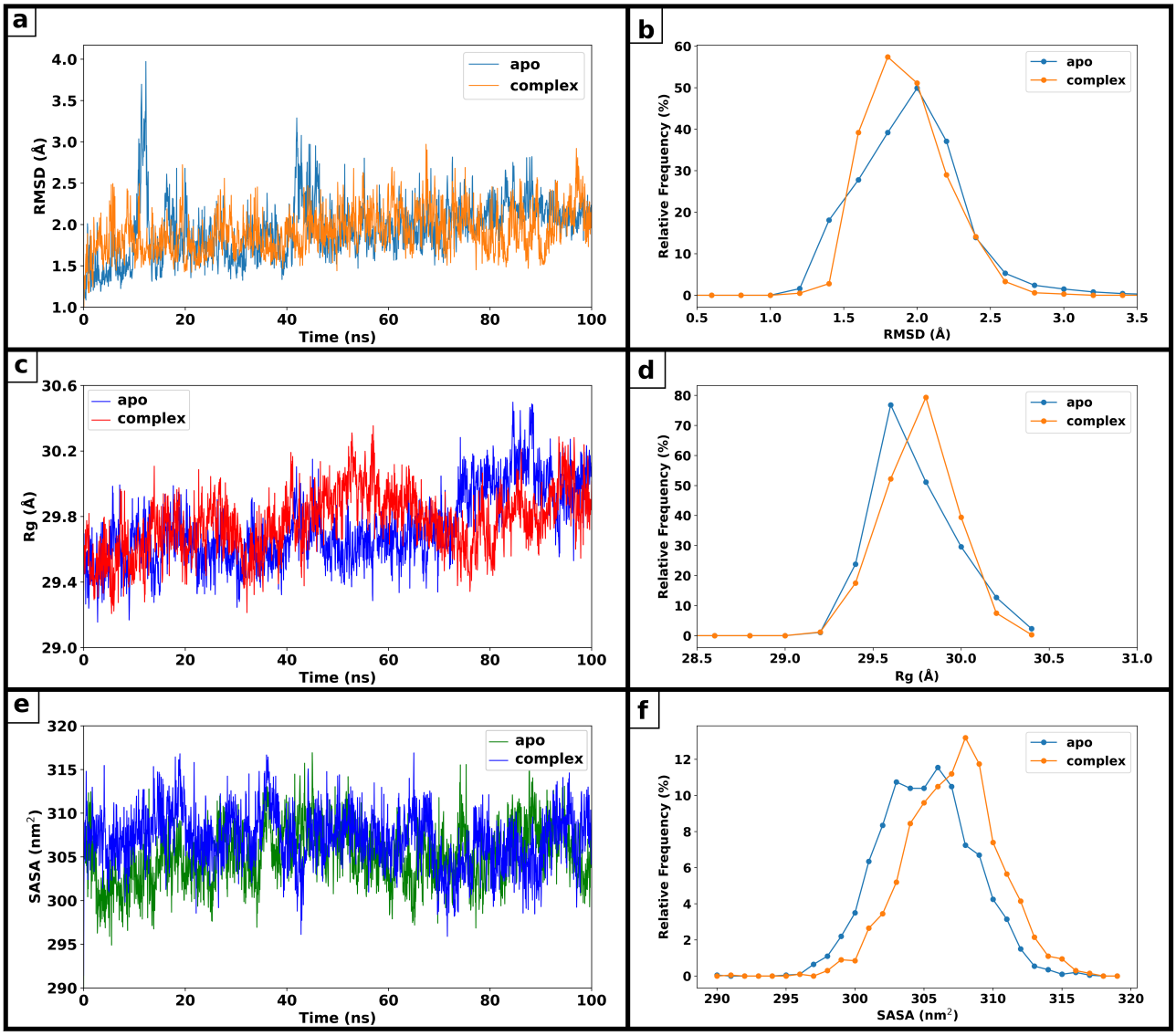

Figure 11. Distributions of RMSD (a, b), R_g (c, d), and SASA (e, f), along with their relative frequencies for both the apo form and dolichin A binding complex of lactoferrin during 100 ns MD simulations.

Stability of a protein-ligand system can be examined by the trajectory analysis during its MD simulations. The time evolution changes of RMSD and its relative frequency in the cases of lactoferrin in apo form as well as liganded with dolichin A have been shown in Figures 11a,b. During

a 100 ns trajectory of the apo form, the average RMSD of the protein backbone is 1.9 ± 0.4 Å with the maximum value of 4.0 Å. The most frequently observed RMSD in the apo form is 2.0 Å. The average RMSD of the protein backbone in dolichin A bound lactoferrin is 1.9 ± 0.3 Å with a maximum value of 3.0 Å, and the most prevalent RMSD is 1.8 Å. Again, the average RMSD of heavy atoms of the ligand with respect to the protein backbone is found to be 2.1 ± 0.3 Å. These outcomes show the stability of both apo and ligand binding forms. Furthermore, dolichin A fits well within the binding pocket of lactoferrin, and there is slightly less deviating conformations of the dolichin A bound protein system in comparison with the apo structure.

The compactness of a protein system is evaluated by calculating R_g of its backbone atoms. Throughout the simulation, both the apo and ligand binding forms consistently exhibit the R_g values of 29.7 ± 0.2 Å and 29.8 Å ± 0.2 Å with the maximum values of 30.5 Å and 30.4 Å, respectively (Figures 11c,d). These results show the compactness of the lactoferrin is nearly consistent after binding with dolichin A.

The impact of solvation on biomolecules is assessed through the calculation of SASA. The SASA of both apo and dolichin A binding forms remain relatively stable, having the values 305 ± 4 nm^2 and 307 ± 3 nm^2, respectively (Figures 11e,f). The maximum SASA values are 316 nm^2 for the apo form and 317 nm^2 for the ligand binding form. There is no significant change in solvent accessibility of lactoferrin after binding with dolichin A.

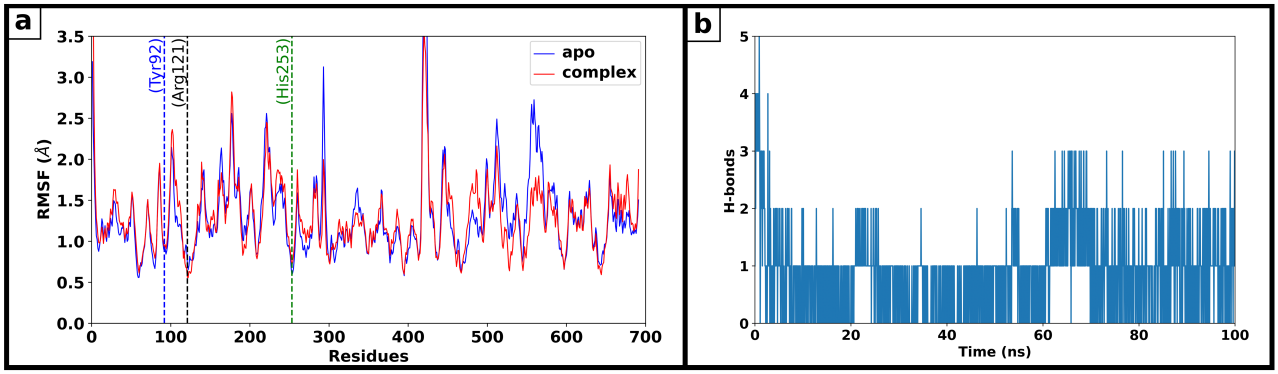

Figure 12. (a) RMSF of the amino acid residues in apo form and dolichin A bound lactoferrin where the metal-oxalate binding active residues are marked with the dotted lines and (b) distribution of H-bonds between lactoferrin and dolichin A during MD simulations.

The flexibility of residues in the protein systems is obtained through RMSF calculation. For the apo and ligand binding forms, the average RMSF of the backbone is observed to be 1.3 ± 0.5 Å with maximum values of 5.4 Å and 5.8 Å, respectively (Figure 12a). Among the active residues, LEU59 and ASP60 in apo form, whereas ARG121 and THR122 in ligand binding form, show the lowest RMSF of 0.56 Å (Table 4S). From the 100 ns trajectory analysis, one can conclude that the lactoferrin appears to be stable throughout the MD simulations.

The distribution of H-bonds between dolichin A and active amino acids of lactoferrin during the 100 ns of MD simulations is illustrated in Figure 12b. In the initial 60 ns, a single H-bond has been observed over the majority of time. During the time interval of 60 to 100 ns, two H-bonds are predominantly observed. The maximum of five H-bonds have been formed between dolichin A and lactoferrin, which

is observed at 0.9 ns of equilibration run.

3.10. MM-GBSA calculations

The post MD free energy of dolichin A in complex with lactoferrin has been analyzed by MM-GBSA calculations. The major contributors to the total binding free energy are van der Waals energy (vdW), electrostatic energy (EEL), polar solvation energy (EGB), and nonpolar solvation energy (ESURF). The total binding free energy contributors of dolichin A in complex with lactoferrin taking all 1000 frames under consideration are illustrated in Figure 13a. The total MM-GBSA free energy written as average ± SD is −17.61 ± 4.03 kcal/mol, where the major contributors are vdW energy (−37.13 ± 2.44 kcal/mol) and electrostatic energy (−23.41 ± 5.56 kcal/mol) are depicted in Table 7. The binding free energies contributed by active residues of lactoferrin and dolichin A are illustrated in Figure 13b. The ligand, dolichin A contributes -10.10 ± 2.57 kcal/mol to the total MM-GBSA free energy. Among all residues, ARG121 and HIS253 show the lowest binding free energies of −1.58 ± 0.76 kcal/mol and −1.14 ± 0.43 kcal/mol, respectively (Table 8). Additionally, Figures 13c-d depict variations in vdW energies and total binding free energies across different trajectories in 100 ns MD simulations. During the simulations, the 33rd frame exhibits the minimum vdW energy of −44.25 kcal/mol, whereas the 862nd frame shows the lowest total binding energy of −29.67 kcal/mol.

Table 7. Average binding free energies of lactoferrin-dolichin A complex using the MM-GBSA method (all values are in kcal/mol).

Van der Waals energy	Electrostatic energy	Polar solvation energy	Non-polar solvation energy	Total binding free energy
−37.13±2.44	−23.41±5.56	48.05±3.48	−5.12±0.20	−17.61±4.03

Table 8. The binding free energies contributed by active amino acid residues of lactoferrin and dolichin A (LIG).

Residues	Average energy ± SD (kcal/mol)
VAL:11	−0.89±0.29
GLU:15	1.88±1.01
PRO:42	−1.06±0.30
THR:58	−0.51±0.30
LEU:59	−0.72±0.19
ASP:60	1.15±0.56
PHE:63	−0.79±0.21
GLU:80	0.71±0.26
ARG:121	−1.58±0.76
PHE:190	−0.60±0.35
TYR:192	−0.73±0.43
HIS:253	−1.14±0.43
LIG:692	−10.10±2.57

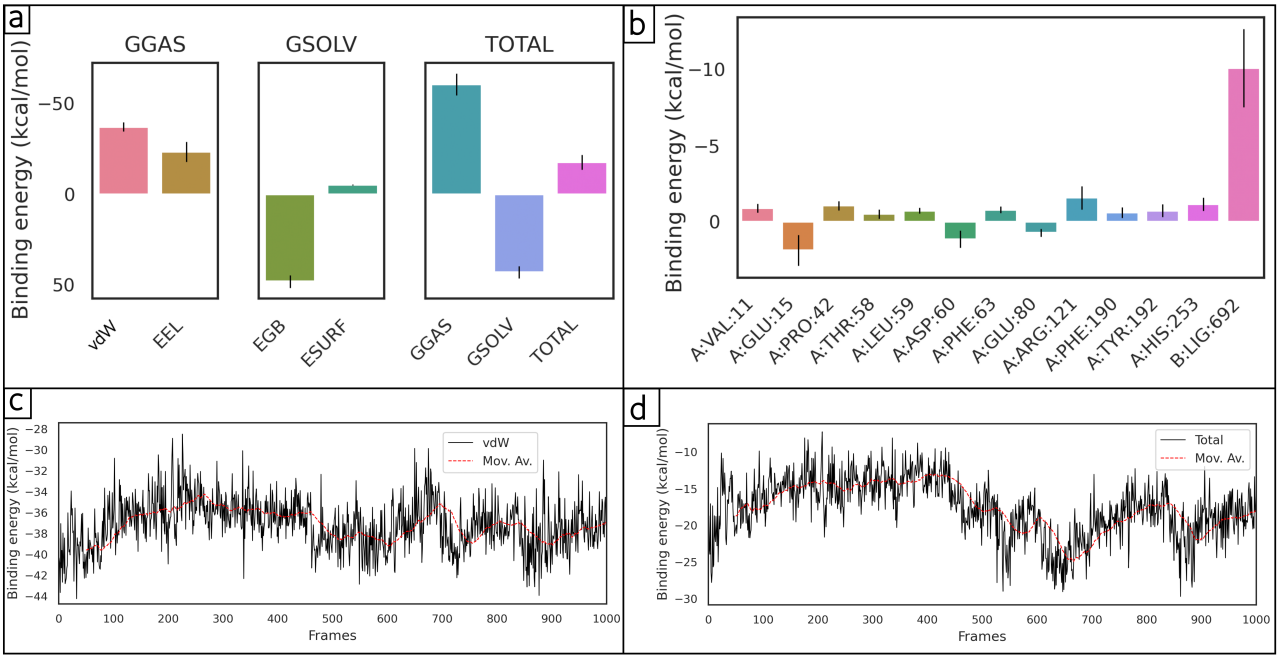

Figure 13. MM-GBSA results of dolichin A in complex with lactoferrin during 100 ns MD simulations: (a) binding free energy contribution by different interactions, (b) binding free energy contributions by active residues and ligand, (c) vdW interaction energy contribution in different frames with moving average, and (d) total binding free energy in different frames with moving average, where vertical lines in bars represent the standard deviations of the corresponding values from 1000 frames.

3.11. Druglikeness and toxicity

Incorporating *in silico* investigation into pharmacokinetics and toxicity assessments of potential drug candidates is helpful for optimizing cost-efficiency, time management, and resource utilization within the realm of drug development [62]. The physicochemical and pharmacokinetic properties, lipophilicity, druglikeness, and toxicity of dolichin A are detailed in Tables 5S - 10S. Dolichin A possesses a molecular weight of 340.37 g/mol (< 500 g/mol), number of H-bond acceptors 5 (< 10), and number of H-bond donors 3 (< 5) (Table 5S). Additionally, dolichin A exhibits lipophilicity (MLogP) value of 1.90 (< 4.15). These findings indicate that dolichin A adheres to Lipinski's rule of five, underscoring its druglike properties [63]. The bioavailability radar (Figure 8S) comprehensively evaluates six critical physicochemical attributes, namely, lipophilicity, size, polarity, solubility, flexibility, and saturation (Tables 5S and 6S), where dolichin A falls entirely within the pink region. This positioning implies a promising potential for dolichin A as a candidate molecule suitable for the drug development [45]. In the BOILED-Egg model, considering lipophilicity (WlogP) and total polar surface area (TPSA), dolichin A is situated within the white region with a blue marker (Figure 9S). This placement implies that the compound possesses high gastrointestinal absorption potential accompanied by active efflux from the central nervous system and the gastrointestinal lumen [45]. Toxicity assessments for dolichin A reveal inactivity with respect to carcinogenicity, hepatotoxicity, nephrotoxicity, and mutagenicity; however, it exhibits activity

concerning immunotoxicity (Table 10S). Additionally, dolichin A falls into category IV with a median lethal dose (LD_{50}) of 500 mg/kg.

4. Conclusions

This research provides a comprehensive understanding of calcium oxalate (the primary constituent of kidney stones) and dolichin A (a chemical found in *M. uniflorum*), employing a multifaceted approach that encompasses FTIR spectroscopy, DFT analysis, molecular docking, molecular dynamics simulations, MM-GBSA, druglikeness, and toxicity prediction. The experimental FTIR spectra of the kidney stone samples exhibit distinct peaks at 1609 ± 1 cm^{-1} and 1314 ± 1 cm^{-1}, which are in close agreement with the calculated FTIR spectrum of calcium oxalate in a water solvent as well as the experimental FTIR spectrum of calcium oxalate monohydrate. Quantum chemical properties including dipole moment, HOMO and LUMO orbital energies, and electrophilicity index suggest that calcium oxalate and dolichin A exhibit their potential for H-bond and nonbonded interactions with lactoferrin. The protein-ligand interactions and conformational stability have been studied using molecular docking and molecular dynamics simulations. Notably, calcium oxalate exhibits a binding energy of −3.86 kcal/mol with lactoferrin. Among the various compounds identified in *M. uniflorum*, dolichin A emerges as a promising inhibitor for lactoferrin, demonstrating the binding energy of −7.78 kcal/mol. Lactoferrin in complex with dolichin A exhibits dynamical stability within the trajectory of 100 ns. The MM-GBSA calculation after molecular dynamics simulations of lactoferrin-dolichin A complex shows the binding energy of −17.61 ± 4.03 kcal/mol with mostly contributed vdW energy of −37.13 ± 2.44 kcal/mol. These results suggest that dolichin A stands as a potential inhibitor of lactoferrin, making it a prospective candidate for the development of a drug targeting calcium oxalate type kidney stone disease. The preclinical experiments are recommended to validate its inhibitory capabilities.

Use of AI tools declaration

The authors declare they have not used Artificial Intelligence (AI) tools in the creation of this article.

Conflict of interest

The authors declare that there are no conflicts of interest.

Ethics approval and consent to participate

This study was conducted with the approval of the Institutional Review Committee of the Institute of Medicine, Tribhuvan University Teaching Hospital, Maharajgunj, Kathmandu, Nepal with an approval number of 117 (6-11) E2 079/080. Informed consent was received from participants or their parents or legal guardians.

Data availability

The data supporting the findings of this study are available within the article and its supplementary materials.

Authors' contributions

A Acharya: Conceived and designed the experiments, analyzed data, and drafted the manuscript
M Khanal: Data analysis, manuscript writing, and revised the manuscript
R Maharjan: Technical support, critical feedback, and revised the manuscript
K Gyawali: Critical feedback and revised the manuscript
BR Luitel: Critical feedback, data analysis, and revised the manuscript
R Adhikari: Critical feedback, data analysis, and revised the manuscript
DD Mulmi: Critical feedback and revised the manuscript
TR Lamichhane: Technical support, critical feedback, data analysis, and revised the manuscript
HP Lamichhane: Critical feedback, data analysis, and revised the manuscript

Acknowledgment

We would like to express our gratitude to Prof. Dr. Rajendra Parajuli and Asst. Prof. Pitamber Shrestha for their invaluable support in providing access to Gaussian 16W. Additionally, we extend our sincere thanks to Dr. Rabindra Tamang, Dr. Purushottam Parajuli, Dr. Anjit Phuyal, and Dr. Milan Gyawali for their unwavering assistance in the collection of samples. Lastly, we are deeply grateful to Mr. Bidit Lamsal and Mr. Yub Narayan Thapa for their support in generating the FTIR spectra. This research is partially supported by the Research Endowment Fund (REF) at Tribhuvan University, Rector's Office, Research Directorate, Kathmandu, Nepal.

References

1. Lameire NH, Bagga A, Cruz D, et al. (2013) Acute kidney injury: an increasing global concern. *Lancet* 382: 170–179. https://doi.org/10.1016/S0140-6736(13)60647-9
2. Ziemba JB, Matlaga BR (2017) Epidemiology and economics of nephrolithiasis. *Investig Clin Urol* 58: 299–306. https://doi.org/10.4111/icu.2017.58.5.299
3. Pak CY, Poindexter JR, Adams-Huet B, et al. (2003) Predictive value of kidney stone composition in the detection of metabolic abnormalities. *Am J Med* 115: 26–32. https://doi.org/10.1016/S0002-9343(03)00201-8
4. Lieske JC, Rule AD, Krambeck AE, et al. (2014) Stone composition as a function of age and sex. *Clin J Am Soc Nephrol* 9: 2141–2146. https://doi.org/10.2215/cjn.05660614
5. Ouyang JM, Zheng H, Deng SP (2006) Simultaneous formation of calcium oxalate (mono-, di-, and trihydrate) induced by potassium tartrate in gelatinous system. *J Crys Growth* 293: 118–123. https://doi.org/10.1016/j.jcrysgro.2006.05.008

6. Rijal R, Sah M, Lamichhane HP, et al. (2022) Quantum chemical calculations of nicotine and caffeine molecule in gas phase and solvent using DFT methods. *Heliyon* 8: e12494. https://doi.org/10.1016/j.heliyon.2022.e12494
7. Aggarwal KP, Narula S, Kakkar M, et al. (2013) Nephrolithiasis: molecular mechanism of renal stone formation and the critical role played by modulators. *BioMed Res Int* 2013: 292953. https://doi.org/10.1155/2013/292953
8. Farmanesh S, Chung J, Sosa RD, et al. (2014) Natural promoters of calcium oxalate monohydrate crystallization. *J Am Chem Soc* 136: 12648–12657. https://doi.org/10.1021/ja505402r
9. Åbrink M, Larsson E, Gobl A, et al. (2000) Expression of lactoferrin in the kidney: implications for innate immunity and iron metabolism. *Kidney Int* 57: 2004–2010. https://doi.org/10.1046/j.1523-1755.2000.00050.x
10. Baker HM, Anderson BF, Brodie AM, et al. (1996) Anion binding by transferrins: importance of second-shell effects revealed by the crystal structure of oxalate-substituted diferric lactoferrin. *Biochemistry* 35: 9007–9013. https://doi.org/10.1021/bi960288y
11. Nageswari P, Swathi K (2023) *In silico* docking and molecular dynamic (MD) simulations studies of selected phytochemicals against human glycolate oxidase (hGOX) and oxalate oxidase (OxO). *Drug Res* 73: 459–464. https://doi.org/10.1055/a-2088-3889
12. Chattaraj B, Nandi A, Das A, et al. (2023) Inhibitory activity of *Enhydra fluctuans* lour. on calcium oxalate crystallisation through *in silico* and *in vitro* studies. *Front Pharmacol* 13: 982419. https://doi.org/10.3389/fphar.2022.982419
13. Pinipay F, Rokkam R, Botcha S, et al. (2023) Evaluating the anti-urolithiasis potential of *Ficus religiosa* seed GC MS evaluated phytoconstituents based on their in-vitro antioxidant properties and in-silico ADMET and molecular docking studies. *Clin Phytosci* 9: 7. https://doi.org/10.1186/s40816-023-00359-2
14. Gautam M, Katoch S, Chahota RK (2020) Comprehensive nutritional profiling and activity directed identification of lead antioxidant, antilithiatic agent from *Macrotyloma uniflorum* (Lam.) Verdc. *Food Res Int* 137: 109600. https://doi.org/10.1016/j.foodres.2020.109600
15. Sharma N, Bisht SS, Gupta S, et al. (2018) Analysis of proteomic diversity and calcium binding protein(s) in seeds of horse gram (*Macrotyloma uniflorum*) cultivars from Uttarakhand. *Int J Pharm Sci Res* 9: 3274–3280. http://dx.doi.org/10.13040/IJPSR.0975-8232.9(8).3274-80
16. Aditya JP, Bhartiya A, Chahota RK, et al. (2019) Ancient orphan legume horse gram: a potential food and forage crop of future. *Planta* 250: 891–909. https://doi.org/10.1007/s00425-019-03184-5
17. Sousa SF, Fernandes PA, Ramos MJ (2006) Protein–ligand docking: current status and future challenges. *Proteins* 65: 15–26. https://doi.org/10.1002/prot.21082
18. Genheden S, Ryde U (2015) The MM/PBSA and MM/GBSA methods to estimate ligand-binding affinities. *Expert Opin Drug Discov* 10: 449–461. https://doi.org/10.1517/17460441.2015.1032936
19. Pan Y, Lu Z, Li C, et al. (2021) Molecular dockings and molecular dynamics simulations reveal the potency of different inhibitors against Xanthine oxidase. *ACS Omega* 6: 11639–11649. https://doi.org/10.1021/acsomega.1c00968

20. Gaussian 16 Revision C.01 Gaussian Inc, Wallingford CT, 2016. Available from: https://gaussian.com/gaussian16/.
21. GaussView Version 6 Semichem Inc, Shawnee Mission KS, 2019. Available from: https://gaussian.com/gaussview6/.
22. O'boyle NM, Tenderholt AL, Langner KM (2008) Cclib: a library for package-independent computational chemistry algorithms. *J Comput Chem* 29: 839–845. https://doi.org/10.1002/jcc.20823
23. Jamróz MH (2013) Vibrational energy distribution analysis (VEDA): scopes and limitations. *Spectrochim Acta Part A* 114: 220–230. https://doi.org/10.1016/j.saa.2013.05.096
24. Waterhouse A, Bertoni M, Bienert S, et al. (2018) SWISS-MODEL: homology modelling of protein structures and complexes. *Nucleic Acids Res* 46: W296–W303. https://doi.org/10.1093/nar/gky427
25. Kawsar SM, Mostafa G, Huq E, et al. (2009) Chemical constituents and hemolytic activity of *Macrotyloma uniflorum* L. *Int J Biol Chem* 3: 42–48. https://doi.org/10.3923/ijbc.2009.42.48
26. Ingle KP, Al-Khayri JM, Chakraborty P, et al. (2020) Bioactive compounds of horse gram (*Macrotyloma uniflorum* Lam.[Verdc.]). In: Murthy, H.N., Paek, K.Y., *Bioactive Compounds in Underutilized Vegetables and Legumes,* Cham: Springer, 1–39. https://doi.org/10.1007/978-3-030-44578-2_36-1
27. Peter JS, Kappagantu A, Thripureshwari V, et al. (2021) *In silico* approach to predict the potential binding affinity of the active ingredient of the *Macrotyloma uniflorum* seed against orphan nuclear receptor. *Res J Pharm Technol* 14: 694–700. http://dx.doi.org/10.5958/0974-360X.2021.00122.0
28. Prasad SK, Singh MK (2015) Horse gram-an underutilized nutraceutical pulse crop: a review. *J Food Sci Technol* 52: 2489–2499. https://doi.org/10.1007/s13197-014-1312-z
29. Kim S, Chen J, Cheng T, et al. (2023) PubChem 2023 update. *Nucleic Acids Res* 51: D1373–D1380. https://doi.org/10.1093/nar/gkac956
30. Dallakyan S, Olson AJ (2015) Small-molecule library screening by docking with PyRx, In: Hempel, J., Williams, C., Hong, C., *Chemical Biology: Methods and Protocols,* New York: Humana Press, 243–250. https://doi.org/10.1007/978-1-4939-2269-7_19
31. Morris GM, Huey R, Lindstrom W, et al. (2009) AutoDock4 and AutoDockTools4: Automated docking with selective receptor flexibility. *J Comput Chem* 30: 2785–2791. https://doi.org/10.1002/jcc.21256
32. Forli S, Huey R, Pique ME, et al. (2016) Computational protein–ligand docking and virtual drug screening with the AutoDock suite. *Nat Protoc* 11: 905–919. https://doi.org/10.1038/nprot.2016.051
33. Cosconati S, Forli S, Perryman AL, et al. (2010) Virtual screening with AutoDock: theory and practice. *Expert Opin Drug Discov* 5: 597–607. https://doi.org/10.1517/17460441.2010.484460
34. Morris GM, Goodsell DS, Halliday RS, et al. (1998) Automated docking using a Lamarckian genetic algorithm and an empirical binding free energy function. *J Comput Chem* 19: 1639–1662. https://doi.org/10.1002/(SICI)1096-987X(19981115)19:14%3C1639::AID-JCC10%3E3.0.CO;2-B

35. Huey R, Morris GM, Forli S (2012) Using AutoDock 4 and AutoDock vina with AutoDockTools: a tutorial. *The Scripps Research Institute Molecular Graphics Laboratory* 10550: 92037.

36. Lamichhane TR, Ghimire MP (2021) Evaluation of SARS-CoV-2 main protease and inhibitor interactions using dihedral angle distributions and radial distribution function. *Heliyon* 7: e08220. https://doi.org/10.1016/j.heliyon.2021.e08220

37. Bell EW, Zhang Y (2019) DockRMSD: an open-source tool for atom mapping and RMSD calculation of symmetric molecules through graph isomorphism. *J Cheminform* 11: 1–9. https://doi.org/10.1186/s13321-019-0362-7

38. The PyMOL Molecular Graphics System, Version 1.8, 2015. Available from: https://pymol.org/.

39. Laskowski RA, Swindells MB (2011) LigPlot+: multiple ligand–protein interaction diagrams for drug discovery. *J Chem Inf Model* 51: 2778–2786. https://doi.org/10.1021/ci200227u

40. Visualizer, Biovia Discovery Studio, Dassault Systemes; San Diego, CA, USA Version v21.1.0.20298, 2021. Available from: https://www.3ds.com/products/biovia/discovery-studio.

41. Abraham MJ, Murtola T, Schulz R, et al. (2015) GROMACS: High performance molecular simulations through multi-level parallelism from laptops to supercomputers. *SoftwareX* 1: 19–25. https://doi.org/10.1016/j.softx.2015.06.001

42. Zoete V, Cuendet MA, Grosdidier A, et al. (2011) SwissParam: a fast force field generation tool for small organic molecules. *J Comput Chem* 32: 2359–2368. https://doi.org/10.1002/jcc.21816

43. Brooks BR, Brooks III CL, Mackerell Jr AD, et al. (2009) CHARMM: the biomolecular simulation program. *J Comput Chem* 30: 1545–1614. https://doi.org/10.1002/jcc.21287

44. Jorgensen WL, Chandrasekhar J, Madura JD, et al. (1983) Comparison of simple potential functions for simulating liquid water. *J Chem Phys* 79: 926–935. https://doi.org/10.1063/1.445869

45. Daina A, Michielin O, Zoete V (2017) SwissADME: a free web tool to evaluate pharmacokinetics, drug-likeness and medicinal chemistry friendliness of small molecules. *Sci Rep* 7: 42717. https://doi.org/10.1038/srep42717

46. Yang H, Lou C, Sun L, et al. (2019) admetSAR 2.0: web-service for prediction and optimization of chemical ADMET properties. *Bioinformatics* 35: 1067–1069. https://doi.org/10.1093/bioinformatics/bty707

47. Banerjee P, Eckert AO, Schrey AK, et al. (2018) ProTox-II: a webserver for the prediction of toxicity of chemicals. *Nucleic Acids Res* 46: W257–W263. https://doi.org/10.1093/nar/gky318

48. Valdés-Tresanco MS, Valdés-Tresanco ME, Valiente PA, et al. (2021) gmx_MMPBSA: a new tool to perform end-state free energy calculations with GROMACS. *J Chem Theory Comput* 17: 6281–6291. https://doi.org/10.1021/acs.jctc.1c00645

49. Lien EJ, Guo ZR, Li RL, et al. (1982) Use of dipole moment as a parameter in drug–receptor interaction and quantitative structure–activity relationship studies. *J Pharm Sci* 71: 641–655. https://doi.org/10.1002/jps.2600710611

50. Barim E, Akman F (2019) Synthesis, characterization and spectroscopic investigation of N-(2-acetylbenzofuran-3-yl) acrylamide monomer: Molecular structure, HOMO–LUMO study, TD-DFT and MEP analysis. *J Mol Struct* 1195: 506–513. https://doi.org/10.1016/j.molstruc.2019.06.015

51. Mishra R, Joshi BD, Srivastava A, et al. (2014) Quantum chemical and experimental studies on the structure and vibrational spectra of an alkaloid–Corlumine. *Spectrochim Acta A* 118: 470–480. https://doi.org/10.1016/j.saa.2013.09.015

52. Fouad R, Adly OM (2021) Novel Cu2+ and Zn2+ nanocomplexes drug based on hydrazone ligand bearings chromone and triazine moieties: structural, spectral, DFT, molecular docking and cytotoxic studies. *J Mol Struct* 1225: 129158. https://doi.org/10.1016/j.molstruc.2020.129158

53. Pearson RG (1988) Absolute electronegativity and hardness: application to inorganic chemistry. *Inorg Chem* 27: 734–740. https://doi.org/10.1021/ic00277a030

54. Geerlings P, De Proft F, Langenaeker W (2003) Conceptual density functional theory. *Chem Rev* 103: 1793–1874. https://doi.org/10.1021/cr990029p

55. Padmanabhan J, Parthasarathi R, Subramanian V, et al. (2007) Electrophilicity-based charge transfer descriptor. *J Phys Chem A* 111: 1358–1361. https://doi.org/10.1021/jp0649549

56. Parr RG, Szentpály L, Liu S (1999) Electrophilicity index. *J Am Chem Soc* 121: 1922–1924. https://doi.org/10.1021/ja983494x

57. Demircioğlu Z, Kaştaş ÇA, Büyükgüngör O (2015) Theoretical analysis (NBO, NPA, Mulliken population method) and molecular orbital studies (hardness, chemical potential, electrophilicity and Fukui function analysis) of (E)-2-((4-hydroxy-2-methylphenylimino) methyl)-3-methoxyphenol. *J Mol Struct* 1091: 183–195. https://doi.org/10.1016/j.molstruc.2015.02.076

58. Pople JA, Schlegel HB, Krishnan R, et al. (1981) Molecular orbital studies of vibrational frequencies. *Int J Quantum Chem* 20: 269–278. https://doi.org/10.1002/qua.560200829

59. Yoshida H, Ehara A, Matsuura H (2000) Density functional vibrational analysis using wavenumber-linear scale factors. *Chem Phys Lett* 325: 477–483. https://doi.org/10.1016/S0009-2614(00)00680-1

60. Abel R, Young T, Farid R, et al. (2008) Role of the active-site solvent in the thermodynamics of factor Xa ligand binding. *J Am Chem Soc* 130: 2817–2831. https://doi.org/10.1021/ja0771033

61. AlRabiah H, Muthu S, Al-Omary F, et al. (2017) Molecular structure, vibrational spectra, NBO, Fukui function, HOMO-LUMO analysis and molecular docking study of 6-[(2-methylphenyl) sulfanyl]-5-propylpyrimidine-2, 4 (1H, 3H)-dione. *Maced J Chem Chem Eng* 36: 59–80. https://doi.org/10.20450/mjcce.2017.1001

62. Bitew M, Desalegn T, Demissie TB, et al. (2021) Pharmacokinetics and drug-likeness of antidiabetic flavonoids: molecular docking and DFT study. *PLoS One* 16: e0260853. https://doi.org/10.1371/journal.pone.0260853

63. Lipinski CA, Lombardo F, Dominy BW, et al. (2012) Experimental and computational approaches to estimate solubility and permeability in drug discovery and development settings. *Adv Drug Deliv Rev* 64: 4–17. https://doi.org/10.1016/j.addr.2012.09.019

AIMS Press